# Differential cross section for neutron scattering from $^{209}$Bi at 37 MeV and the weak particle-core coupling

Zuying Zhou, Xichao Ruan, Yanfeng Du, Bujia Qi, Hongqing Tang, and Haihong Xia
*China Institute of Atomic Energy, P.O. Box 275-46, Beijing 102413, China*

R. L. Walter, R. T. Braun,* C. R. Howell, W. Tornow, and G. J. Weisel†
*Department of Physics, Duke University, Durham, North Carolina 27708, USA and*
*Triangle Universities Nuclear Laboratory, Durham, North Carolina 27708, USA*

M. Dupuis and J. P. Delaroche
*CEA, DAM, DIF, F-91297 Arpajon, France*

Zemin Chen, Zhenpeng Chen, and Yingtang Chen
*Department of Physics, Tsinghua University, Beijing 100084, China*
(Received 28 May 2010; published 3 August 2010)

Differential scattering cross-section data have been measured at 43 angles from 11° to 160° for 37-MeV neutrons incident on $^{209}$Bi. The primary motivation for the measurements is to address the scarcity of neutron scattering data above 30 MeV and to improve the accuracy of optical-model predictions at medium neutron energies. The high-statistics measurements were conducted at the China Institute of Atomic Energy using the $^{3}$H$(d,n)^{4}$He reaction as the neutron source, a pulsed deuteron beam, and time-of-flight (TOF) techniques. Within the resolution of the TOF spectrometer, the measurements included inelastic scattering components. The sum of elastic and inelastic scattering cross sections was computed in joint optical-model and distorted-wave Born approximation calculations under the assumption of the weak particle-core coupling. The results challenge predictions from well-established spherical optical potentials. Good agreement between data and calculations is achieved at 37 MeV provided that the balance between surface and volume absorption in a recent successful model [A. J. Koning and J. P. Delaroche, Nucl. Phys. A **713**, 231 (2003)] is modified, thus suggesting the need for global optical-model improvements at medium neutron energies.

DOI: 10.1103/PhysRevC.82.024601 PACS number(s): 25.40.Dn, 28.20.Cz, 24.10.Ht, 27.80.+w

## I. INTRODUCTION

For over a half century, the nuclear optical model (OM) has offered a phenomenological analysis of nuclear scattering that not only has yielded significant physical insight but also has had enormous practical value. One variant of the OM, the dispersive optical model (DOM), provides a consistent representation for both bound and scattering states [1]. However, a significant pitfall of phenomenological models is that they are faced with ambiguities among certain tunable parameters. One important ambiguity concerns the tradeoff between the volume absorption term, $W_V$, and the surface absorption term, $W_D$, at medium energies.

An earlier DOM study of $n + {}^{209}$Bi and $n + {}^{208}$Pb by the Triangle Universities Nuclear Laboratory (TUNL) adopted an energy dependence for $W_D(E)$, which resulted in relatively large values of $W_D$ at neutron energies between 30 and 80 MeV [2]. Although this work provided good fits to the data then available to us, it used values of $W_D$ that were significantly larger than those used in traditional OMs. This motivated us, in a later DOM sensitivity study, to adopt an energy dependence of $W_D(E)$ that could produce lower values of $W_D$ between 30 and 80 MeV [3]. However, our study showed that, lacking sufficient and reliable differential data in this region, our database did not favor either the modified or the original potential representation. The test model using lower $W_D$ values between 30 and 80 MeV featured higher values for the volume imaginary term, $W_V$, and vice versa for the original model.

The main reason why it is difficult to place constraints on the energy dependencies of the $W_V$ and $W_D$ potential depths, and resolve this ambiguity, is the lack of high-precision differential cross-section data in the medium-energy ($E_n >$ 30 MeV), high-angle ($\theta_{\text{c.m.}} > 60°$) regime. For the $n + {}^{209}$Bi and $n + {}^{208}$Pb scattering systems, the only data available for differential cross section, $\sigma(\theta)$, are the 30.3- and 40.0-MeV $^{208}$Pb data of Ref. [4]. Unfortunately, there are not many facilities in the world with quasimonenergetic neutron sources in this energy regime. The China Institute of Atomic Energy has a tandem accelerator that reaches terminal voltages up to 13 MV and a tritium gas target system, both of which were used to collect the present $^{209}$Bi$(n,n)$ $\sigma(\theta)$ high-statistics data at 37 MeV. These new measurements are timely since the large-scale OM analysis of Ref. [5] suggests a deficiency in the overall normalization of the 40.0-MeV data of Ref. [4].

*Permanent address: Department of Computer Science Duke University, Durham, NC 27708-0129.

†Permanent address: Department of Physics, Penn State Altoona, Altoona, PA 16601.

 

Owing to the limitations of the time-of-flight (TOF) technique, neutron scattering at medium energy cannot compete with proton scattering as a high-accuracy spectroscopy tool. Within the resolution of the TOF spectrometer, the measured elastic-scattering cross section can include components arising from the excitation of low-lying levels. In the present study, such components have been accounted for using the weak particle-core coupling, which has proved successful for structure studies in the $^{208}$Pb region [6].

The paper is organized as follows. In Sec. II the experimental setup is described. Section III focuses on the data acquisition as well as finite-geometry and multiple-scattering corrections. In Sec. IV our experimental results are corrected for the contamination by inelastic scattering and compared to OM calculations. Finally, in Sec. V we note the opportunity of extending the present measurements to other spherical nuclei, thus enlarging the database in the medium-energy regime, which can be used to improve neutron scattering models and make their predictions more accurate.

## II. EXPERIMENTAL SETUP

The experimental target area is shown in Fig. 1. The 4-MHz pulsed deuteron beam was provided by the HI-13 tandem accelerator. The 37-MeV neutrons were produced via the $^3$H$(d,n)^4$He reaction ($Q$ value = 17.6 MeV) employing a gas cell. Typically, the deuteron beam current delivered to the gas cell was 2.5 $\mu$A, resulting in neutron fluxes of about $10^8$ neutrons per steradian per second at zero degrees [7,8].

A schematic diagram of the gas target system, consisting of a tritium gas cell and a helium gas cell, is shown in Fig. 2. The body of the tritium cell is a stainless-steel cylinder that is 4.6 cm long and 1.2 cm in diameter and has a wall thickness of 0.2 mm. The cell was sealed by a Mo foil of 15 mg/cm$^2$ and by two O-rings, one made of indium and the other of rubber. It was filled with tritium gas to a pressure of 2.2 atm. Gold metal was used as a beam stop and as a liner. The helium gas cell (located upstream in the beam line in relation to the tritium cell) is a tube with flanges at both ends for mechanical connection and vacuum sealing. It is 2.3 cm long and 1.2 cm in diameter and is held at a pressure of about 0.2 atm. One end of the helium gas cell shared the first Mo foil with the tritium gas cell and the other end was sealed by a second Mo foil, this one with thickness of 10 mg/cm$^2$, and a rubber O-ring.

Two transducers were used to monitor the pressure of the tritium and helium cells. If the pressure moved out of preset ranges, the transducers produced an alarm signal and immediately closed a fast-acting valve located 15 m upstream from the tritium target. A special chimney and ventilation tube were constructed for the tritium target and, after the experiment, the tritium gas was stored in a uranium oven.

The primary neutrons of the $^3$H$(d,n)^4$He reaction were monitored by a designated TOF spectrometer (the detector in Fig. 1 with the longer flight path). The neutron yields from this monitor were used to normalize the other detectors from run to run. As a check, the monitor was compared to the beam current. The two measurements were consistent throughout the experiment.

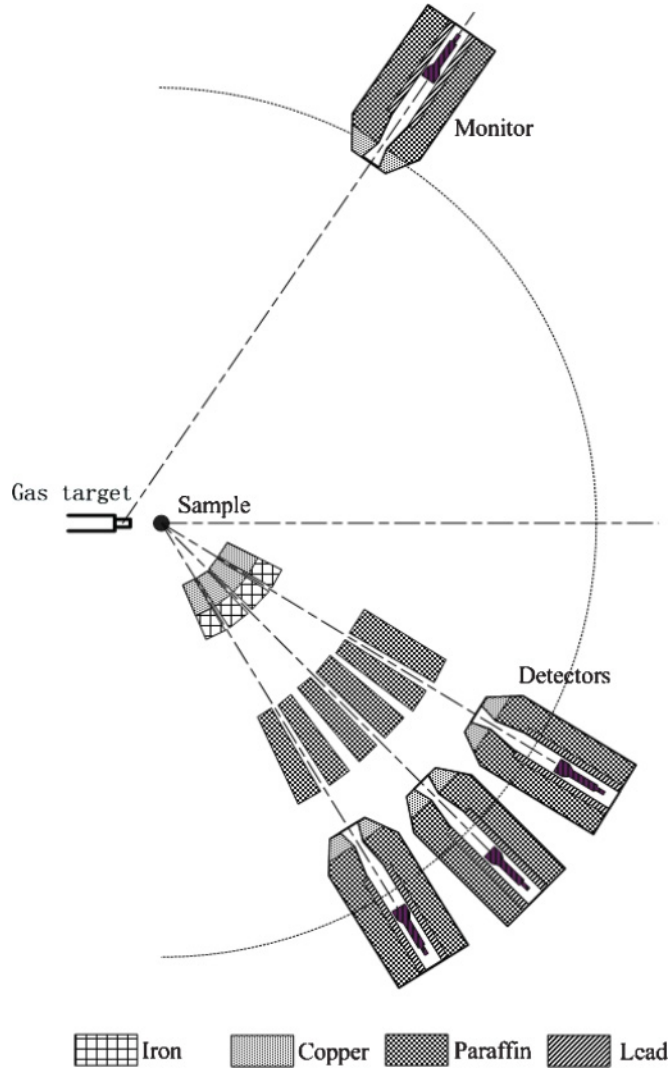


FIG. 1. The fast-neutron TOF spectrometer at the China Institute of Atomic Energy.

The metallic bismuth sample, a 25 × 35 mm cylinder, was placed 20 cm away from the center of the tritium gas target. For laboratory angles less than $\theta_{lab} = 26^\circ$, for which the cross section is large and varies greatly with angle, we used a smaller sample measuring 15 × 35 mm. The secondary neutrons

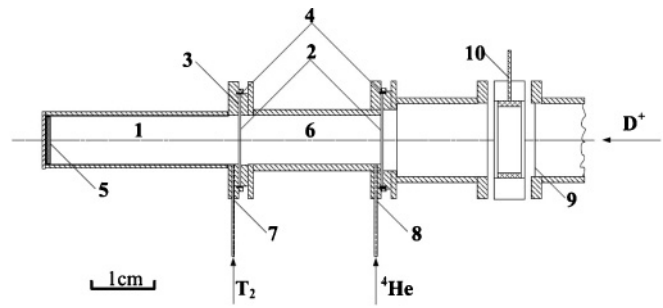


FIG. 2. Cross-section view of the tritium gas cell system. The labels indicate (1) tritium gas cell, (2) Mo foil, (3) indium O-ring, (4) rubber O-ring, (5) gold beam stop, (6) $^4$He gas cell, (7) tritium gas tube, (8) $^4$He gas tube, (9) Ta diaphram, and (10) electron suppressor.

(those scattered from the sample) were measured by all three neutron detectors of the TOF spectrometer simultaneously [9]. The neutron detectors were liquid scintillators (ST-451, an equivalent of NE-213), of diameter 10.4 cm and thickness 5.0 cm, coupled to a photomultiplier tube. Each detector was well collimated and massively shielded, as is shown in Fig. 1. The flight path of the scattered neutrons was 609, 654, or 515 cm, depending on which of the three neutron detectors was used. For the measurements at angles less than 30°, only one detector was used because of the greater difficulty of shielding from the primary neutrons. In addition, the neutrons coming directly to the detector from the tritium gas cell were attenuated by an additional iron shadow bar placed between the source and the first collimator.

We estimate the total energy resolution of our experimental setup to be 2.7 MeV. This contains four potential contributions. The most important is due to the time resolution of the TOF spectrometer itself, which we estimate to be no greater than 2.5 ns. Because $E_d = 20$ MeV (to produce $E_n = 37$ MeV via the source reaction), the energy spread owing to the gas cell is so small (less than 0.05 MeV) that it can be ignored. The diameter of the $^{209}$Bi sample (2.5 cm) causes a time spread of about 0.3 ns. Finally, the thickness of the detectors (5.0 cm) contributes about 0.6 ns to the time spread. These contributions are added in quadrature to give a total time spread of about 2.6 ns, corresponding to a FWHM neutron energy spread of about 2.7 MeV.

The angular distribution of scattered neutrons from the $^{209}$Bi sample was measured at 43 laboratory angles in steps of 3° to 5°. At each angle, both sample-in and sample-out measurements were taken to determine the background.

To obtain absolute differential cross-section data, we determined the neutron flux per area at the location of the bismuth target. To accomplish this, we removed the target and set the three main detectors in turn at zero degrees and measured the source neutron yield, $M(0^\circ)$, from the $^3$H$(d,n)^4$He reaction. For these zero-degree measurements, the beam current was not allowed to exceed 150 nA, to keep the dead time as low as possible. The yield over the angles subtended by the detector can be expressed as

$$M(0^\circ) = Qn_T\sigma_{dT}(0^\circ)\frac{A\varepsilon_i}{(d+l)^2}, \tag{1}$$

where $Q$ is the number of incident deuterons, $n_T$ is the areal number density of $^3$H in the gas cell, $A$ is the area of the neutron detector, $\varepsilon_i$ is the detector efficiency, $d$ is the sample to detector distance, and $l$ is the source to sample distance. Because the angle subtended by the detectors was less than ±0.5°, we used the differential cross section of the source reaction for zero degrees, $\sigma_{dT}(0^\circ)$.

The neutron flux reaching the sample can be written as

$$N(0^\circ) = Q\frac{n_T\bar{\sigma}_{dT}}{l^2}, \tag{2}$$

where $\bar{\sigma}_{dT}$ is the cross section for the $^3$H$(d,n)^4$He reaction, averaged over the angle subtended by the sample (±3.58° for the large scatterer and ±2.15° for the small scatterer). The value of $Q$ in Eq. (2) is the same as that in Eq. (1) since we rescaled to an equal number of monitor counts. We took the cross section for the neutron source reaction from DROSG-2000 [10]. Combining Eqs. (1) and (2) gives the neutron flux per area at the location of the bismuth target as

$$N(0^\circ) = M(0^\circ)\frac{\bar{\sigma}_{dT}}{\sigma_{dT}(0^\circ)}\frac{(d+l)^2}{l^2A\varepsilon_i}. \tag{3}$$

## III. DATA ANALYSIS

The elastically scattered neutron yields, $N(\theta)$, were extracted from the sample-in and sample-out measurements and the neutron flux incident on the scatterer as follows. All TOF spectra were filtered using pulse-shape discrimination to reject the $\gamma$-ray background. A software threshold for the neutron detectors was set at 20 times the $\gamma$-ray Compton edge for $^{137}$Cs, corresponding to a neutron energy of about 15 MeV. Both the sample-in and sample-out spectra were first normalized to a constant neutron flux, as determined by the designated TOF spectrometer monitoring the source neutrons.

A sample TOF spectrum is shown for $\theta_{\text{c.m.}} = 39.4^\circ$ in Fig. 3 (with time increasing from right to left). After normalization, the sample-out spectra were subtracted from the sample-in spectra, thus producing the "difference spectra." A gate (shown as the dashed vertical lines in Fig. 3) was placed on the elastic neutron peak to determine the $N(\theta)$ values. The difference spectra sometimes showed a small residual background. On the right (low TOF) side, the background was always consistent with zero. On the left (high TOF) side, small background features sometimes intruded into the elastic peak. These were removed by estimating their shape graphically and were no more than 1% of the total counts.

The differential cross section at each scattering angle was obtained with the following expression:

$$\sigma(\theta) = \frac{N(\theta)}{N(0^\circ)}\frac{d^2l^2}{(d+l)^2}\frac{\varepsilon_i}{\varepsilon}\frac{1}{N_s}, \tag{4}$$

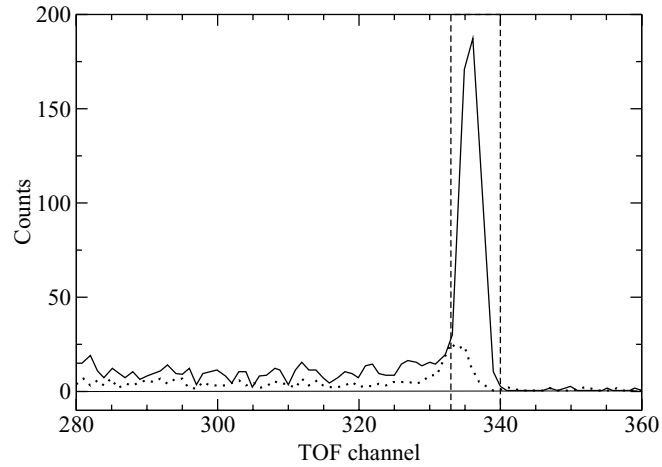


FIG. 3. Sample TOF spectrum for $\theta_{\text{c.m.}} = 39.4^\circ$. Time increases from right to left. The sample-in spectrum is shown by the solid curve and the the sample-out spectrum is shown as the dotted curve. The two vertical dashed lines are the gates used to determine the yield.

where $N(\theta)$ is the yield within the elastic peak for that particular angle; $N(0^\circ)$ is the yield of the primary neutrons of the $^3$H$(d,n)^4$He reaction over the angular region subtended by the sample [for the same monitor counts as that of the $N(\theta)$ measurement] as determined by Eq. (3); $d$, $l$, and $\varepsilon_i$ are defined in the discussion following Eq. (1); $N_s$ is the number of nuclei in the sample (which was fully illuminated); and $\varepsilon$ is the neutron detector efficiency for the scattered neutrons. Detector efficiency corrections were not needed since the energy of the secondary neutrons for $n + ^{209}$Bi remains virtually constant with angle.

After completing these steps, the data still contained experimental artifacts owing to the finite size of the scattering sample. We used the Monte Carlo (MC) computer code STREUER [11] to simulate the experimental details, including flux-attenuation, multiple-scattering, and finite-geometry effects in the $^{209}$Bi sample. The MC library included data for the $^3$H$(d,n)^4$He source reaction (using the code NEUYIE of DROSG-2000) as well as for $^{209}$Bi. The total cross section data for $^{209}$Bi were taken from the JENDL/HE library [12]. As a first guess for the $^{209}$Bi $\sigma(\theta)$ data at 37 MeV, the library used a fit to the raw experimental data. The MC simulation then produced experimental/calculated ratios for the $\sigma(\theta)$ data. These were used to modify the $^{209}$Bi library and the MC code was iterated until the ratios reached the desired precision.

Figure 4(a) shows the raw experimental $\sigma(\theta)$ data as the pluses and the MC-corrected data as the open circles. The final, corrected data are also listed in Table I. The solid curve in Fig. 4(a) is a Legendre polynomial fit to the open circles.

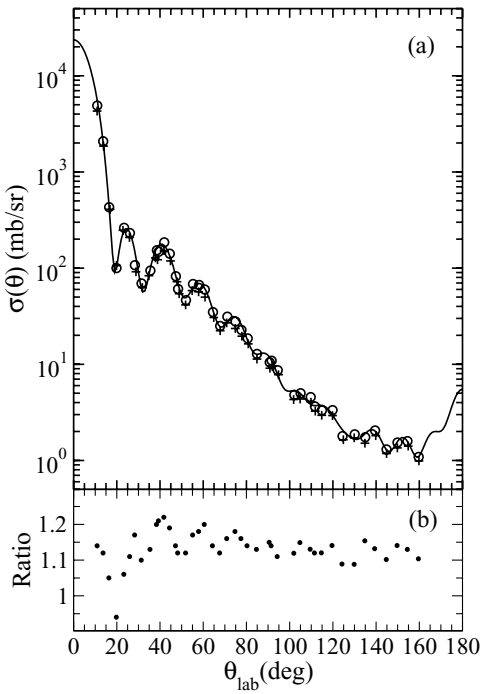


FIG. 4. Monte Carlo corrections. (a) The pluses show the raw $^{209}$Bi$(n,n)$ $\sigma(\theta)$ data at 37 MeV; the open circles show the MC-corrected data. The solid curve is a Legendre polynomial fit to the open circles. (b) The ratio between the MC-corrected data and the raw data.

TABLE I. Final $^{209}$Bi$(n,n)$ differential cross section data, $\sigma(\theta)$, at $E_n = 37$ MeV, with absolute uncertainties, $\Delta\sigma(\theta)$, which include the statistical and dead-time uncertainties discussed in the text.

| $\theta_{\text{c.m.}}$ (deg) | $\sigma(\theta)$ (mb/sr) | $\Delta\sigma(\theta)$ (mb/sr) |
|---|---|---|
| 10.9 | 4890 | 230 |
| 13.7 | 2079 | 90 |
| 16.5 | 429 | 23 |
| 19.9 | 100 | 10 |
| 23.4 | 263 | 16 |
| 26.1 | 231 | 17 |
| 28.4 | 107 | 11 |
| 31.4 | 69.2 | 6.3 |
| 35.5 | 94.3 | 7.8 |
| 38.6 | 153.3 | 8.6 |
| 39.4 | 148.0 | 8.2 |
| 42.0 | 185.4 | 5.6 |
| 44.6 | 141.3 | 5.8 |
| 47.3 | 82.2 | 5.8 |
| 48.4 | 60.6 | 4.6 |
| 52.0 | 46.4 | 3.1 |
| 55.3 | 68.4 | 3.1 |
| 58.1 | 66.8 | 4.2 |
| 60.7 | 59.9 | 3.3 |
| 64.5 | 34.9 | 2.4 |
| 67.8 | 25.0 | 1.8 |
| 71.1 | 31.3 | 3.0 |
| 75.0 | 27.8 | 3.0 |
| 77.7 | 22.7 | 2.4 |
| 80.6 | 18.6 | 1.3 |
| 84.9 | 12.8 | 1.0 |
| 90.8 | 10.5 | 1.2 |
| 91.7 | 10.9 | 1.2 |
| 94.5 | 8.65 | 0.92 |
| 102.2 | 4.81 | 0.74 |
| 105.0 | 5.00 | 0.73 |
| 109.7 | 4.56 | 0.65 |
| 111.7 | 3.64 | 0.47 |
| 114.9 | 3.31 | 0.41 |
| 119.8 | 3.34 | 0.53 |
| 124.5 | 1.79 | 0.31 |
| 130.1 | 1.87 | 0.32 |
| 135.0 | 1.74 | 0.37 |
| 139.6 | 2.05 | 0.33 |
| 144.9 | 1.30 | 0.22 |
| 149.9 | 1.54 | 0.23 |
| 154.6 | 1.59 | 0.19 |
| 159.7 | 1.09 | 0.17 |

The fit required a highest $L$ value of $26\hbar$ and satisfies Wick's limit (which is 23,620 mb/sr), as do the optical-model predictions discussed in the next section. Figure 4(b) displays the ratio of the MC-corrected data to the raw experimental data, which typically has values in the range from 1.1 to 1.2.

The uncertainties of Table I include the following sources. For the three main neutron detectors, the statistical uncertainties were 4%–9% for the angle range 11° to 70° and

10%–20% for the angle range 75° to 160°. For the 0° measurement, the statistical uncertainty was less than 1%. For the monitor neutron detector, statistical uncertainties for the scattering measurements were less than 1% and less than 2% for the 0° measurement. The uncertainties of Table I also include the uncertainty of the dead-time correction, which was no more than 2%. (All of the listed scattering angles are subject to an uncertainty of ±0.2°.) The size of the uncertainties, especially small for $\theta_{\text{c.m.}} < 70°$, reflects the high yields collected during these long measurements. Therefore, the present data offer the opportunity for a critical assessment of scattering models at medium energy.

## IV. OPTICAL-MODEL ANALYSES

Initial calculations with the DOM of Ref. [2] and the more recent global optical model of Ref. [5] showed that the data of Table I were somewhat higher than the model predictions in the angle region between $\theta_{\text{c.m.}} = 60°$ and 120°. This indicated the possibility that our data were contaminated by inelastic scattering. Because our energy resolution is about 2.7 MeV, it is likely that our TOF gates included contributions from the low-lying $^{209}$Bi excited states.

Low-lying states in even-odd nuclei close to the doubly-magic $^{208}$Pb nucleus form two groups. The first includes levels having relatively pure shell-model configurations whereas the second includes multiplets arising from the weak coupling of valence particles or holes to collective excitations of the $^{208}$Pb core. In $^{209}$Bi the proton $h_{9/2}$ single-particle level (the $^{209}$Bi ground state) couples to the collective $3^-$ level of $^{208}$Pb to form a septuplet of states with angular momentum $I^\pi = \frac{3}{2}^+$, $\frac{5}{2}^+$, $\frac{7}{2}^+$, $\frac{9}{2}^+$, $\frac{11}{2}^+$, $\frac{13}{2}^+$, and $\frac{15}{2}^+$ at a centroid energy of $E_x(3^-) =$ 2.615 MeV in $^{208}$Pb. This is a typical example of the weak particle-core coupling [13], a scheme unequivocally identified in Coulomb excitation [14] and high-energy-resolution $(p,p')$ and $(d,d')$ scattering measurements [6,15].

The excited states of importance to our present OM analyses, with energy up to about $E_x = 2.7$ MeV, are taken from the Brookhaven database [16]. The experimental energies, spins, and parities used for the present OM analyses are as follows. The single-proton states have $E_x =$ 0.896 MeV ($I^\pi = \frac{7}{2}^-$) and 1.609 MeV ($\frac{13}{2}^+$). The members of the particle-core septuplet are 2.493 MeV ($\frac{3}{2}^+$), 2.564 MeV ($\frac{9}{2}^+$), 2.583 MeV ($\frac{7}{2}^+$), 2.600 MeV ($\frac{11}{2}^+$), 2.601 MeV ($\frac{13}{2}^+$), 2.617 MeV ($\frac{5}{2}^+$), and 2.741 MeV ($\frac{15}{2}^+$). All these levels have been identified and their excitation strengths measured in $(p,p')$ scattering experiments [6].

In a first step, we performed optical-model calculations for $(p,p')$ scattering using the Bechetti-Greenlees potential [17] and assuming the validity of the distorted-wave Born approximation (DWBA), both of which served well in previous calculations at 35 MeV [6]. We adopted the code ECIS [18] for the calculations in which complex form factors have been used for real and imaginary central $L = 2\hbar$ and $L = 3\hbar$ potential transitions. Coulomb excitation has been considered in the early stage of our calculation but ignored later as it did not impact our results. The present calculations provide angular distributions that are identical to those published in Ref. [6].

From this analysis, we deduced the deformation lengths $\delta_L = \beta_L R_V$ for the $L = 2\hbar$ and $L = 3\hbar$ transitions, with $R_V$ as the radius of the real central potential. The deformation lengths were built so that they take on identical values for real and imaginary transition potentials associated with the same $L$ values. For the single-proton states, we found $\delta_L =$ 0.0854 fm for $E_x = 0.896$ MeV, $L = 2\hbar$, and found $\delta_L =$ 0.1777 fm for $E_x = 1.609$ MeV, $L = 3\hbar$. For the septuplet, we found $\delta_L = 0.7915$ fm for $E_x = 2.615$ MeV, $L = 3\hbar$.

We next performed analyses of the present neutron-scattering cross section taking advantage of these results. The $(n,n)$ and $(n,n')$ scattering calculations at 37 MeV have been conducted using the Koning-Delaroche potential [5]. We assumed that the deformation lengths do not depend on the probe. This is a good approximation since no core polarization is expected in doubly-closed-shell nuclei [19]. Elastic and DWBA inelastic scattering calculations have been performed under the same assumptions as previously. Finally, we formed the sum of the $(n,n)$ and $(n,n')$ scattering cross sections.

The results are shown in Fig. 5, where the solid circles are the data of Table I. The lower (black) curve shows the $\sigma(\theta)$ prediction of the OM potential of Ref. [5] for elastic scattering only. The upper (red) curve shows the sum of the $(n,n)$ and $(n,n')$ components. The addition of the inelastic scattering cross sections serve to raise the OM prediction. This worsens the fit at the forward angles but improves it significantly beyond 60°.

To further improve the agreement between our prediction and the data, we performed new calculations in which the

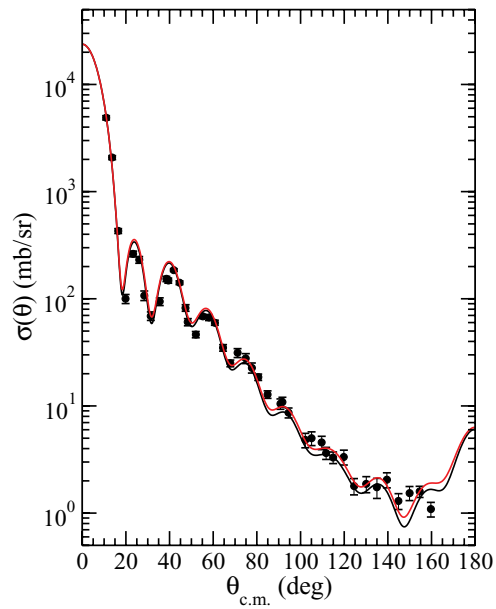


FIG. 5. (Color online) The $^{209}$Bi$(n,n)$ data at 37 MeV of Table I (solid circles) compared to the OM prediction of Ref. [5] for the elastic channel only (lower, black curve) and to the same prediction but with the addition of inelastic scattering up to $E_x < 2.7$ MeV (red curve).

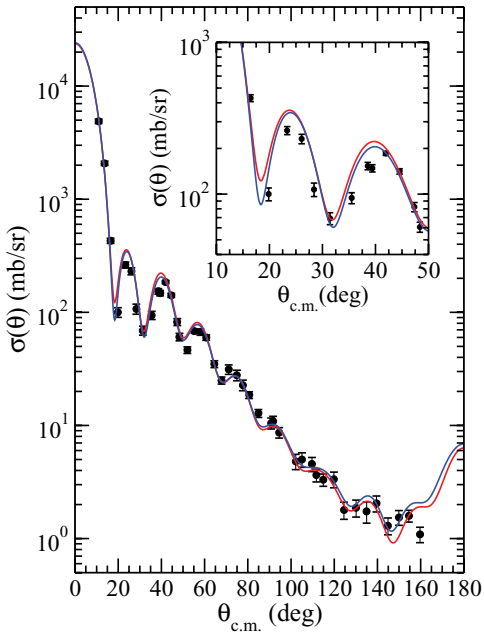


FIG. 6. (Color online) The $^{209}$Bi$(n,n)$ data at 37 MeV of Table I (solid circles) compared to the nominal prediction of the global OM of Ref. [5] (at the back angles, the lower, red curve) and the modified version of the OM (blue curve), as described in the text. Both curves display the sum of elastic and inelastic cross sections.

depths of the real and imaginary central potentials were altered from their nominal values in Ref. [5]. We first tried changing the values of the real central potential by ±0.50 MeV. The nominal values proved to be the best; otherwise the prediction for the first diffraction minimum did not match the data. We then modified the absorptive components, taking care not to spoil the good fit to total cross section, $\sigma_T$, achieved previously. An optimum fit to the differential data was achieved by increasing the volume-imaginary potential $W_V$ by 1.0 MeV (2.879 MeV was replaced by 3.879 MeV) and by decreasing the surface-imaginary potential $W_D$ by 1.0 MeV (5.488 MeV was replaced by 4.488 MeV). This modification changed the predictions of $\sigma_T$ by less than 1%. In Fig. 6, one can see that the modified model (the blue curve, which is higher at the backward angles and lower at the forward angles) does a better job at representing the differential data (especially at the forward angles; see insert) than the prediction of the nominal model (the red curve, which is the same as the red curve of Fig. 5).

Our modification of the OM of Ref. [5] constitutes a significant redistribution of strengths between the surface and volume absorption. This redistribution was quantified by calculating the volume integrals $J_{WV}/A$ and $J_{WD}/A$ for the volume-imaginary and surface-imaginary potentials, respectively. We found that the volume term went up, from 24.49 MeV fm$^3$ for the nominal model to 33.00 MeV fm$^3$ for the optimum model. Meanwhile, the surface term went down, from 37.52 MeV fm$^3$ to 30.68 MeV fm$^3$. The ratio of $J_{WD}/A$ to $J_{WV}/A$ changed from 1.53 for the nominal potential to 0.93 for the modified model. In the modified model, note that the absorption is equally distributed over the volume and surface components, to within 10%.

## V. SUMMARY AND OUTLOOK

We have presented new $\sigma(\theta)$ measurements for $^{209}$Bi$(n,n)$ at 37-MeV incident neutron energy, as part of an effort to address the lack of neutron nucleus differential scattering data above 30 MeV. The new data are some of the best available for high-$Z$ targets in this energy regime, featuring angular measurements up to $\theta_{\text{c.m.}} = 160^\circ$ and good statistics. Further data of similar quality will be needed at medium neutron energies to further address the issues that we have raised.

We have drawn two conclusions from the present analysis. First, we have demonstrated the usefulness of the weak particle-core coupling for several collective excitations in the $^{208}$Pb core. Although our differential cross-section measurements were contaminated by inelastic scattering to low-lying levels because of the finite energy resolution of our experimental setup, we were able to evaluate these contributions. The validity of the weak particle-core coupling is well established in the region of $^{209}$Bi, beginning with the high-resolution differential scattering measurements for proton scattering at 35 MeV of Ref. [6]. Without recourse to this coupling scheme, our present conclusions regarding the neutron OM properties would have been weaker.

Second, we have concluded that the balance between surface and volume absorption for the established global neutron-nucleus optical-model potential of Ref. [5] is not at its best at $E_n = 37$ MeV. Our OM calculations have revealed that the fit to scattering data is benefited by an increase in the volume-imaginary central potential depth and a decrease in the surface-imaginary depth, thus confirming the suspicions of the authors of Ref. [3]. Our analysis indicates that the volume and surface bulk potential absorptions take on similar values at 37 MeV incident energy, about 10 MeV lower than inferred from Ref. [5].

Differential neutron scattering measurements around 40 MeV provide key information for mapping the interplay between surface and volume absorptive potentials. This cannot be established unambiguously by relying exclusively on $\sigma_T$ within the accuracy of the measurements. But, as our present analysis shows, relying on differential scattering measurements at medium energies requires having control over the inelastic scattering components that inevitably arise from the finite experimental energy resolution. In the present study, the inelastic scattering cross-section contributions were relatively small, but for nuclei departing from double-shell closures, the collectivity content of low-lying excited states may grow significantly. In these instances, we suggest that an estimate of inelastic scattering cross sections be made on the basis of previous $(p,p')$ and Coulomb-excitation measurements (and model analyses) and core polarization, which impacts scattering from single-closed-shell nuclei at and away from the $\beta$-stability line [20].

The present work therefore opens the way to improving the accuracy of nuclear reaction-model predictions. It would be interesting to implement this structure information in new

$(n,n')$ scattering model calculations for $^{209}$Bi and observe their impact on reaction-channel predictions of model calculations that have heretofore ignored the direct excitation of low-lying discrete excited states [21]. Extending differential scattering measurements to other spherical targets such as $^{54}$Fe, $^{120}$Sn, and $^{140}$Ce would be a valuable asset for improving the energy dependencies of the potential depths in the medium-energy regime for phenomenological OMs.

**ACKNOWLEDGMENTS**

This work was supported by the US Department of Energy, under Grant No. DE-FG02-97ER41033, by the United States–China Cooperative Science Program of the US National Science Foundation, under Grant No. 19275026, and by the China National Natural Science Foundation. J.P. Delaroche thanks TUNL for its generous support.

[1] C. Mahaux and R. Sartor, Adv. Nucl. Phys. **20**, 1 (1991).
[2] G. J. Weisel, W. Tornow, C. R. Howell, P. D. Felsher, M. AlOhali, M. L. Roberts, R. K. Das, R. L. Walter, and G. Mertens, Phys. Rev. C **54**, 2410 (1996).
[3] G. J. Weisel and R. L. Walter, Phys. Rev. C **59**, 1189 (1999).
[4] R. P. DeVito, Ph.D. thesis, Michigan State University, 1979.
[5] A. J. Koning, and J. P. Delaroche, Nucl. Phys. A **713**, 231 (2003).
[6] W. T. Wagner, G. M. Crawley, and G. R. Hammerstein, Phys. Rev. C **11**, 486 (1975).
[7] Y. M. Tian *et al.*, Nucl. Instrum. Methods **244**, 39 (1986).
[8] H. Tang *et al.*, in *Proceedings of the International Conference on Nuclear Data for Science and Technology, Trieste, Italy, 19–24 May, 1997*, edited by G. Reffo, A. Ventura, and C. Grandi (Editrice Compositori, Bologna, Italy, 1997), Part 1, p, 429.
[9] J. Sa *et al.*, At. Energ. Sci. Technol. **26**, 1 (1992).
[10] M. Drosg, DROSG-2000 computer code, [http://www-nds.iaea.org/drosg2000.html].
[11] STREUER computer code, developed by PTB, Braunschweig, Germany, with modifications made by Dankwart Schmidt for neutron energies up to 50 MeV (2003).
[12] Japanese Evaluated Nuclear Data Library, [http://wwwndc.jaea.go.jp/jendl/jendl.html].
[13] B. Mottelson, Rev. Mod. Phys. **48**, 375 (1976); A. Bohr and B. Mottelson, *Nuclear Structure* (Benjamin, Reading, MA, 1975), Vol. II, p. 570; I. Hamamoto, Phys. Rep. **10**, 63 (1974).
[14] R. A. Broglia, J. S. Lilley, R. Perazzo, and W. R. Phillips, Phys. Rev. C **1**, 1508 (1970).
[15] J. Ungrin, R. M. Diamond, P. O. Tjom, and B. Elbek, Mat. Fys. Medd. K. Dan. Vidensk. Selsk. **38**(8), (1971).
[16] National Nuclear Data Center, Brookhaven National Laboratory, [http://www.nndc.bnl.gov/ensdf/].
[17] F. D. Becchetti Jr. and G. W. Greenlees, Phys. Rev. **182**, 1190 (1969).
[18] J. Raynal, Notes on ECIS94, CEA Saclay Report No. CEA-N-2772, 1994.
[19] D. E. Bainum, R. W. Finlay, J. Rapaport, J. D. Carlson, and W. G. Love, Phys. Rev. C **16**, 1377 (1977).
[20] A. M. Bernstein, Adv. Nucl. Phys. **3**, 325 (1969); V. R. Brown and V. A. Madsen, Phys. Rev. C **11**, 1298 (1975); V. A. Madsen, V. R. Brown, and J. D. Anderson, *ibid.* **12**, 1205 (1975); A. M. Bernstein, V. R. Brown, and V. A. Madsen, Phys. Lett. B **71**, 48 (1977); V. A. Madsen and V. R. Brown, Phys. Rev. Lett. **52**, 176 (1984); L. A. Riley *et al.*, Phys. Rev. C **72**, 024311 (2005).
[21] L. C. Mihailescu, C. Borcea, A. J. Koning, A. Pavlik, and A. J. M. Plompen, Nucl. Phys. A **799**, 1 (2008).